Journal of Alloys and Compounds 526 (2012) 11–21

Contents lists available at SciVerse ScienceDirect

Journal of Alloys and Compounds

journal homepage: www.elsevier.com/locate/jallcom

Study of the annealing temperature effect on the structural and luminescent properties of $SrWO_4$:Eu phosphors prepared by a non-hydrolytic sol–gel process

P.F.S. Pereira [a], A.P. de Moura [a], I.C. Nogueira [a], M.V.S. Lima [a], E. Longo [b], P.C. de Sousa Filho [c], O.A. Serra [c], E.J. Nassar [d], I.L.V. Rosa [a,*]

[a] Universidade Federal de São Carlos/UFSCar, Via Washington Luís, Km 235, ZIP 13565-905, São Carlos, SP, Brazil
[b] Universidade Estadual Paulista Júlio de Mesquita Filho/UNESP, R. Francisco Degni, S/N, ZIP 14801-907, Araraquara, SP, Brazil
[c] Universidade de São Paulo/FFCLRP-USP, Via Bandeirantes, 3900, ZIP 14040-901, Ribeirão Preto, SP, Brazil
[d] Universidade de Franca/UNIFRAN, Via Dr. Armando Salles de Oliveira, 201, ZIP 14404-600, Franca, SP, Brazil

ARTICLE INFO

Article history:
Received 28 October 2011
Received in revised form 18 January 2012
Accepted 13 February 2012
Available online xxx

Keywords:
Non-hydrolytic sol–gel
Strontium tungstate
Scheelite
Europium

ABSTRACT

In this paper, we investigate the influence of temperature on the structural and luminescent properties of Eu^{3+}-doped strontium tungstate oxide ($SrWO_4$) prepared by the non-hydrolytic sol–gel route. X-ray diffraction (XRD) analyses showed that the $SrWO_4$:Eu scheelite type structure was formed in a unique phase at 900 and 1000 °C over 2 h. Raman spectra indicated only one type of [WO_4] tetrahedron. The optical properties were investigated by ultraviolet–visible (UV–vis) absorption spectroscopy and photoluminescence (PL) measurements at room and liquid N_2 temperatures. PL study showed $^5D_0 \rightarrow {}^7F_2$ electric dipole transition is dominant when Eu^{3+} occupies a non-centrosymmetric environment. The (FEG-SEM) images indicated that an increase in the annealing temperature contributed to the coalescence process which promoted the growth of aggregated particles of a polydisperse nature. A qualitative analysis of the powders obtained by dispersive X-ray detector (EDS) indicated that the samples are composed of Sr, W and O while Eu^{3+} ion was not observed due to it low concentration.

1. Introduction

Optical properties of trivalent rare earth (RE^{3+}) ions in tungstate materials with a scheelite structure have been widely investigated [1]. There has been significant interest in studying the interactions between (RE^{3+}) ions in solids. This research is attributed in part to the importance of rare earth doped materials in optical system applications and also to advances in experimental techniques which allow the investigation of the properties of the interactions in greater detail than was previously possible [2]. The motivation for these studies is based on: (i) their technological applications as phosphor materials in fluorescent lamps, cathode ray tubes and X-ray intensifying screens [1]; (ii) stimulated Raman scattering (SRS) operations which have been thoroughly studied to develop laser devices emitting in new spectral regions [3]; and (iii) display devices, transparent luminescence layers or markers on metal, ceramics and plastics as well as biomaterials [4].

Trivalent RE ions are used to dope inorganic oxides as a probe to investigate local centers and energy promoting changes in optical behavior or improving the capacitance response of these materials which facilitates their use as high frequency ultrasonic transducers [5]. $Eu^{3+}$is one of the most interesting ions to study with site selection spectroscopy techniques because its optical properties are very sensitive to its local environment. The intensities and splitting of the spectral lines provide useful information concerning the local site symmetry, sizes of cations and properties of the chemical bonding [2]. Eu^{3+} is a preferable choice as an activator ion with red emission via a $^5D_0 \rightarrow {}^7F_2$ transition at 616 nm when the ion is present in a non-centrosymmetric site which has been used in most commercial red phosphors. The intensities of Eu^{3+} emissions at around 394 and 465 nm are improved in these materials as compared with most other Eu^{3+} doped phosphors [6]. Some Eu^{3+} activated tungstates and molybdates with a scheelite structure have efficient red-light emission in the near-UV region [7,8]. These phosphors are relatively stable and have strong absorption in the near-UV region; therefore, they are promising candidates as a red component for white LED emission devices (WLEDs) [7].

However, most of these materials were prepared by a traditional solid-state method which usually requires high temperatures, a lengthy heating process and subsequent grinding. The grinding process usually damages the phosphor surfaces which results in the loss of emission intensity [6]. In addition, aggregation and inhomogeneous shapes are also unavoidable and can inhibit the absorption of the excitation energy and thereby reduce the emission intensity. Therefore, a simple and economical method for

* Corresponding authors at: Department of Chemistry, LIEC-UFSCar, Caixa Postal 676, 13560-905 São Carlos, SP, Brazil. Tel.: +55 16 3351 9308; fax: +55 16 3351 8214.
E-mail address: ilvrosa@ufscar.br (I.L.V. Rosa).

0925-8388/$ – see front matter © 2012 Elsevier B.V. All rights reserved.
doi:10.1016/j.jallcom.2012.02.083

making high-quality phoshors is desirable. The sol–gel method has some advantages over the conventional solid-state reaction method such as easy stoichiometric control, good homogeneity, lower annealing temperatures and a shorter heating time; the prepared samples show a small size and narrow particle size distribution. Phosphor materials must have a narrow size distribution, non-agglomeration properties and spherical morphology for good luminescent characteristics [6,9–13].

In this paper, $SrWO_4$ powders doped with Eu^{3+} were synthesized by the non-hydrolytic sol–gel route; the powders were annealed at 600, 800, 900 and 1000 °C for 2 h. The obtained powders were analyzed by X-ray diffraction (XRD) and Raman spectroscopy. The images were analyzed by FEG-SEM. A qualitative analysis of the powders obtained was performed by using an energy dispersive X-ray detector (EDS). Optical properties were investigated by UV–vis absorption spectroscopy and photoluminescence (PL) measurements at room and liquid N_2 temperatures.

2. Experimental

2.1. Non-hydrolytic sol–gel synthesis of RE^{3+} doped $SrWO_4$

$SrWO_4$:Eu powders were prepared by the non-hydrolytic sol–gel route [9–13]. A methanolic europium chloride solution (0.1 mol L^{-1}) was prepared from its oxide (Eu_2O_3, 99.99%, Aldrich) which was first dissolved in concentrated HCl followed by the evaporation of excess acid and the addition of anhydrous methanol. 1.0 g of tungsten hexachloride (WCl_6, Aldrich, 99.99%) was dissolved in 200 mL of methanol (MeOH) which was used as a solvent and oxygen donor. In a subsequent step, acetylacetone (Hacac, Aldrich, 99.99%) in a 1:3 molar ratio related to the WCl_6 was mixed into this solution to prevent precipitation of the tungsten species. Strontium chloride ($SrCl_2$, Aldrich, 99.99%) was added in a 1:1 W:Sr molar ratio with the addition of 1.0% in mol of Eu^{3+} in relation to the Sr^{2+} ions. The mixture was kept in reflux for 4 h under an argon atmosphere. After the reaction, the mixture was cooled and aged overnight at room temperature; the solvent was then removed under vacuum. The $SrWO_4$:Eu powder was dried and annealed at 600, 800, 900 and 1000 °C for 2 h.

2.2. Measurements

The powders were structurally characterized by XRD using a Rigaku-DMax/2500PC (Japan) with Cu Kα radiation (λ = 1.5406 Å) in the 2θ range from 15° to 75° with a 0.02° s^{-1} increment. Raman spectra were recorded using the Horiba Jobin Yvon model LabRAM HR 800 mm. High resolution Raman spectra were taken with a He–Ne laser at 632.81 nm (model CCD DU420A-OE-325) operating in the 50–1000 cm^{-1} range. UV–vis spectra were measured using Cary 5G (USA) equipment in the reflection mode. The powder morphologies were verified using a FEG-SEM (Supra 35-VP, Carl Zeiss, Germany). EDS results were obtained using a Noran System 7 model (Noran System Six version software). PL data were obtained under continuous Xe lamp (450 W) excitation in a SPEX Triax 550 Fluorolog 3 spectrofluorometer at room and liquid N_2 temperatures. The detection was performed with a Peltier-cooled SPEX Synapse CCD. The emission was collected at 90° from the excitation beam. The Eu^{3+} lifetime was evaluated through the decay curve set of the excitation emission wavelength at 394 and 616 nm, respectively.

3. Results and discussion

3.1. XRD

Fig. 1 shows a typical XRD pattern for $SrWO_4$:Eu powders prepared by the non-hydrolytic sol–gel route which were calcined at 600, 800, 900 and 1000 °C for 2 h.

Diffraction peaks can be used to evaluate the long-range structural order or the periodicity of the material [14,15]. According to Fig. 1, the samples treated at 600 and 800 °C for 2 h showed a phase mixture which can be ascribed to tungsten(VI) oxychloride or tungsten(VI) oxide ($WOCl_4$ or WO_3), respectively. Diffractograms indicate that the formation of a pure scheelite-like $SrWO_4$:Eu does not occur at these temperatures [16]. For the samples treated at 900 and 1000 °C, the peaks indicate that pure scheelite-like $SrWO_4$:Eu powders were well crystallized which suggests a long-range ordered structure [15,17–19]. All diffraction peaks can be indexed as a pure tetragonal structure with a space group of $I4_1/a$ (no. 88, C_{4h}^6) with cell parameters of $a = b = 5.416$ Å and $c = 11.951$ Å

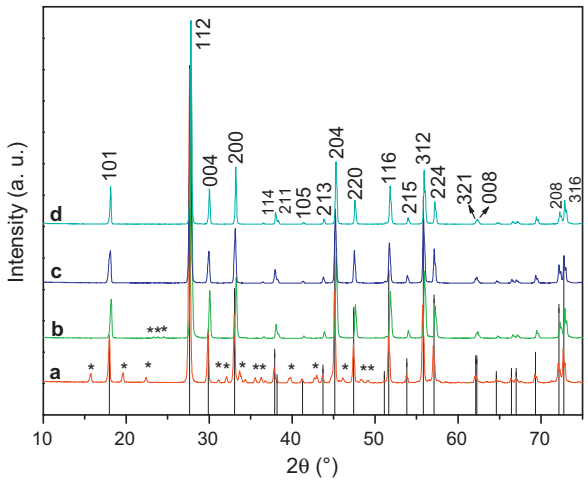

Fig. 1. XRD of $SrWO_4$:Eu samples annealed at (a) 600 °C, (b) 800 °C, (c) 900 °C and (d) 1000 °C for 2 h. JCPDS (85-0587).

and a cell volume of 350.56 $Å^3$ (JCPDS 85-0587) [20,21]. The corresponding lattice sample parameters were obtained with a general structure analysis system (GSAS) program and are listed in Table 2. These powder phosphors fundamentally maintain characteristics of a scheelite structure which obviously are not affected by doped Eu^{3+} ions [22]. The highest intensity peak is visible at ca. $2\theta \approx 27°$ (1 1 2). Fig. 1 does not show any differences regarding scheelite diffraction patterns which indicates that doped Eu^{3+} ions do not change the lattice structure [23,24]. Due to different valence states and the difference in the ion size between W^{6+} (0.042 nm) and Eu^{3+} (0.107 nm), Eu^{3+} is expected to occupy the Sr^{2+} (0.113 nm) site in this phosphor [23] which is reasonable because the electronic densities of Eu^{3+} and Sr^{2+} at their coordination numbers are analogous [25] (see Fig. 4). In this structure, W^{6+} occupies tetrahedral sites constructed with O^{2-} which compose the $[WO_4]^{2-}$ clusters. Sr^{2+} is eight coordinated with O^{2-} and forms a distorted dodecahedron for the S_4 point group [3,8,26,27]; Eu^{3+} doping ions occupy the Sr^{2+} site [8]. The absence of the peaks assigned to the europium oxide (Eu_2O_3) indicates that $SrWO_4$:Eu compounds were formed (see Fig. 1). This absence is strong verification of successful substitution of Sr^{2+} by the Eu^{3+} ions in the tungstate framework.

Average crystallite sizes were estimated by Scherrer's equation using the full width at half maximum (FWHM) of the most intense peak (1 1 2). As reported in the literature, Scherrer's equation (Eq. (1)) is described as follows:

$$D = \frac{0.9\lambda}{B\ \cos\theta} \quad (1)$$

where D is average crystallite sizes, λ is the X-ray wavelength (0.15406 nm), θ is the Bragg angle and B is the FWHM [17,28]. Based on this equation, average crystallite sizes for the four $SrWO_4$:Eu powder samples were estimated in the range from 40 to 53 nm.

3.2. Rietveld refinement analysis

The Rietveld analysis was carried out on crystalline $SrWO_4$:Eu samples heat treated at 900 and 1000 °C for 2 h (see Figs. 2 and 3).

This analysis was performed using the fullprof package and assuming a $I4_1/a$ space group for a scheelite type tetragonal structure. In this scheelite type tetragonal structure, Sr, Eu, W and O atoms occupy 4b, 4a and 16f sites with angles ($\alpha = \beta = \gamma = 90°$), respectively. A typical example of this analysis is shown in Figs. 2 and 3 which depicts the experimental and calculated XRD patterns obtained by the refinement of the $SrWO_4$ phase doped with Eu^{3+}. Coefficients of the Rietveld analysis are listed in Table 1.

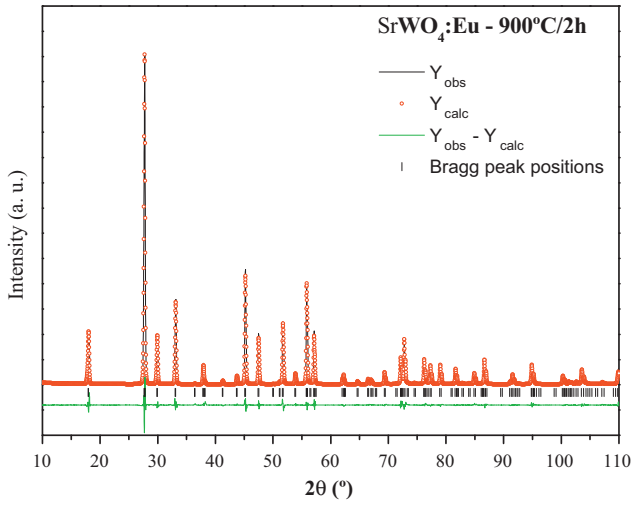

Fig. 2. Rietveld plot for crystalline $SrWO_4$:Eu heat treated at 900 °C for 2 h.

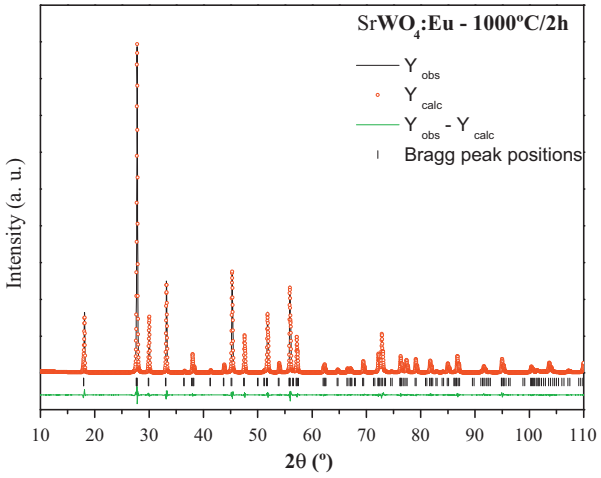

Fig. 3. Rietveld plot for crystalline $SrWO_4$:Eu heat treated at 1000 °C for 2 h.

Table 1
Coefficients of the Rietveld refinement for $SrWO_4$:Eu samples treated at 900 and 1000 °C for 2 h.

$SrWO_4$:Eu	R_{wp} (%)	R_{Bragg} (%)	χ^2
900 °C	9.45	3.72	7.648
1000 °C	7.74	2.42	5.395

Table 4
Bond length (W—O) and angles of the $[WO_4]$ clusters.

$SrWO_4$:Eu	α	β	Bond length (Å)
900 °C for 2 h	104.1	120.8	1.88
1000 °C for 2 h	107.3	114.0	1.74

Figs. 2 and 3 present minor deviations ($Y_{obs} - Y_{calc}$), R_{wp}, R_{Bragg} and χ^2 (see Table 1) which are attributed to the good quality of the structural refinement [28]. These results indicate that $SrWO_4$:Eu samples treated at 900 and 1000 °C showed the desired crystalline phase; no phase mixture was observed which confirms results obtained by conventional XRD (see Fig. 1).

Table 2 shows lattice parameter values, angle and cell volume of the unit cell for $SrWO_4$:Eu obtained by Rietveld refinement.

Table 2 shows Rietveld refinement data for $SrWO_4$:Eu powders heat treated at 900 and 1000 °C which confirm a tetragonal structure pertaining to the $I4_1/a$ space group. Lattice parameters and cell volumes of the 900 and 1000 °C treated samples did not indicate significant changes. However, only a slight environmental distortion was noticed which is in agreement with the refinement from the GSAS and the JCPDS card no. 85-0587.

Table 3 lists atomic coordinates for Sr, Eu, W and O atoms obtained by the Rietveld refinement used to model the tetragonal $SrWO_4$:Eu unit cells which was heat treated at 900 and 1000 °C for 2 h. According to these data, the environment distortion is verified mainly in the *x* atomic coordinate since its value is 0.2698 for the O atom in the sample heated at 900 °C while in the sample heated at 1000 °C, this coordinate was determined as 0.2343.

3.3. Unit cell representation for $SrWO_4$:Eu

Fig. 4 illustrates the schematic representation of a $SrWO_4$:Eu tetragonal unit cell with a $I4_1/a$ space group which was modeled by using the Diamond program (Version 3.2 DEMO) [29,30].

The construction of a $1 \times 1 \times 1$ unit cell of $SrWO_4$:Eu (see Fig. 4) employed the structural parameters and atomic coordinates listed in Tables 2 and 3. In Fig. 4 the Sr^{2+} and Eu^{3+} cations are coordinated to the eight oxygen atoms considered as $[SrO_8]$ and $[EuO_8]$ groups which form a distorted dodecahedron geometry [18,31]. The W atoms are coordinated to four oxygens which are $[WO_4]$ groups with a slight distortion in the tetrahedral geometry [18,32]. This behavior was verified through the different bond angle values between oxygen atoms when the heat treatment changes from 900 to 1000 °C (see Table 4).

Tables 4 and 5 show angle values and bond lengths of $[WO_4]$ and $[SrO_8]$ clusters determined from Fig. 4 by simulation (Diamond

Table 2
Lattice parameters and volume cell of the samples $SrWO_4$:Eu heat treated at 900 and 1000 °C for 2 h.

$SrWO_4$:Eu	Lattice parameters (Å)		Unit cell angle (°)	Cell volume (Å^3)
	$a = b$	c	$\alpha = \beta = \gamma$	
900 °C	5.419	11.961	90	351.246
1000 °C	5.417	11.957	90	350.949
JCPDS	5.416	11.951	90	350.559

Table 3
Atomic coordinates used to model the tetragonal $SrWO_4$:Eu unit cell, heat treated at 900 and 1000 °C for 2 h.

Atom	Site	$SrWO_4$:E (900 °C)			$SrWO_4$:E (1000 °C)		
		x	*y*	*z*	*x*	*y*	*z*
O	16f	0.2698	0.1164	0.0475	0.2343	0.1172	0.0455
Sr	4b	0	0.2500	0.6250	0	0.2500	0.6250
Eu	4b	0	0.2500	0.6250	0	0.2500	0.6250
W	4a	0	0.2500	0.1250	0	0.2500	0.1250

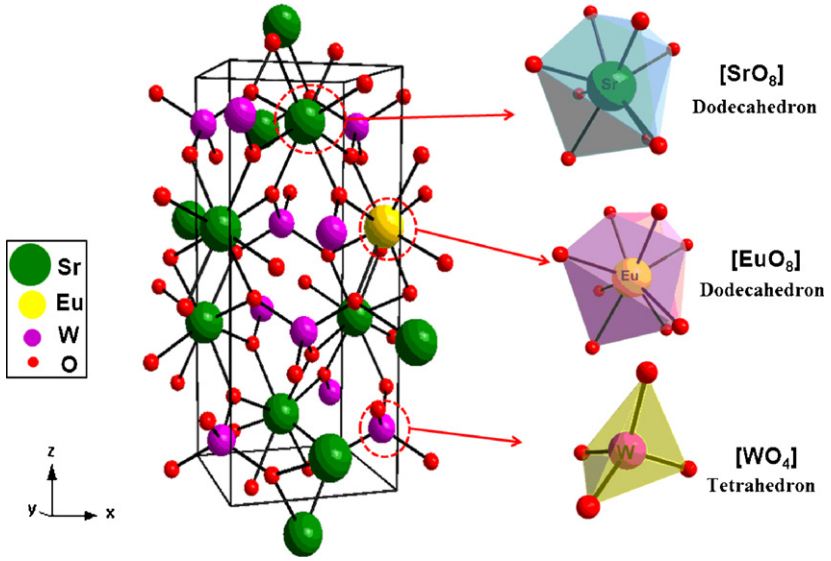

Fig. 4. Illustrations of the $SrWO_4$:Eu coordination geometries of the $[WO_4]$/$[SrO_8]$/$[EuO_8]$ clusters treated at 1000 °C for 2 h.

Table 5
Bond length and angles of the Sr—O clusters.

$SrWO_4$:Eu	α	β	γ	δ	ε	ζ	η	θ	Bond length (Å)
900 °C for 2 h	69.9	71.3	73.6	76.5	97.8	132.0	136.9	146.5	2.52; 2.51
1000 °C for 2 h	67.8	73.0	76.6	79.1	97.5	128.0	137.7	148.6	2.60; 2.63

program) through the Rietveld refinement data. A small variation between angle values and bond lengths groups is observed. The results showed that the $SrWO_4$:Eu powder has a small degree of distortion at short range in $[WO_4]$ and $[SrO_8]$ groups. The addition of 1.0% Eu^{3+} to $SrWO_4$ and the annealing temperature effect can promote some differences in the bond length due to group rearrangement inside the lattice matrix.

The crystal structure of $SrWO_4$:Eu is characterized by a covalent/ionic character between Sr—O and Eu—O bonds whereas the W—O bonds have a covalent nature along $[WO_4]$ clusters [18,33].

3.4. Micro-Raman spectroscopy analysis

Raman-active phonon modes can be employed to estimate the short-range structural order of the material [14]. Vibrations of AWO_4 are classified into two types (internal and external modes) [6] which occur due to weak coupling between the ionic group $[WO_4]$ and the Sr^{2+} cation [28]. The first mode belongs to the vibration inside $[WO_4]$ molecular units where the centers of mass are stationary. The second mode is a lattice phonon which corresponds to the motion of A^{2+} cations and rigid molecular units. In free space, $[WO_4]$ tetrahedra have a T_d symmetry [34,35]. Their vibrations are composed of four internal modes (υ_1 (A1), υ_2 (E), υ_3 (F2) and υ_4 (F2)), one free rotational mode ($\upsilon_{f.r}$ (F1)) and one translational mode (F2) [34]. In a lattice space, the $[WO_4]$ symmetry is reduced to S_4, and all degenerate vibrations are split [34,35] due to the crystal field effect [34].

Stronger Raman-active vibrational modes indicate a strong interaction between ions which is due mainly to stretching and bending vibrations of shorter metal–oxygen bonds within anionic groups [21].

Fig. 5 shows Raman spectra in the frequency ranging from 50 to 1000 cm^{-1} for $SrWO_4$:Eu powders processed by the non-hydrolytic sol–gel route and treated at 600, 800, 900 and 1000 °C for 2 h.

These spectra show 11 different energy vibrational modes which are higher symmetric modes and anti-symmetric stretching between O—W—O; the lower energy modes are the torsion modes between W—O and Sr—O. Among them, there are three A_g vibrations (922.61, 337.93 and 190.33 cm^{-1}), four B_g (839.75, 373.77, 337.93 and 76.05 cm^{-1}) and five E_g (800.95, 384.10, 238.40, 135.09 and 102.62 cm^{-1}) [35]. The Raman peak at 922.61 cm^{-1} could be assigned as υ_1 of the W—O symmetric stretching while the peak at 337.93 cm^{-1} is assigned as υ_2 of the O—W—O symmetric bending. The peaks at 839.75 and 800.95 cm^{-1} are designated as υ_3 of the W—O anti-symmetric stretching, and peaks at 373.77 and 384.10 cm^{-1} are designated as υ_4 of the O—W—O anti-symmetric bending [36]. The peaks located at 238.40, 190.33, 135.09 and 102.62 cm^{-1} as well as at 76.05 cm^{-1} are assigned to rotational (A_g, E_g) and translational modes (B_g) [37]. External peak modes are localized at a range from 76.05 to 135.09 cm^{-1} which corresponds

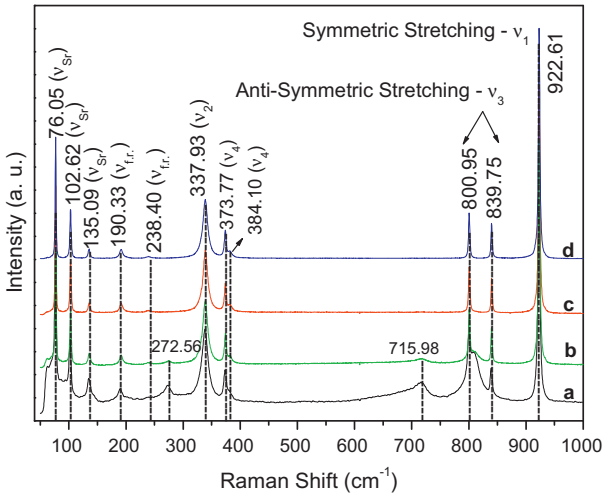

Fig. 5. Room temperature depolarized Raman spectra of $SrWO_4$:Eu powders processed by the non-hydrolytic sol–gel route and treated at (a) 600 °C, (b) 800 °C, (c) 900 °C and (d) 1000 °C for 2 h.

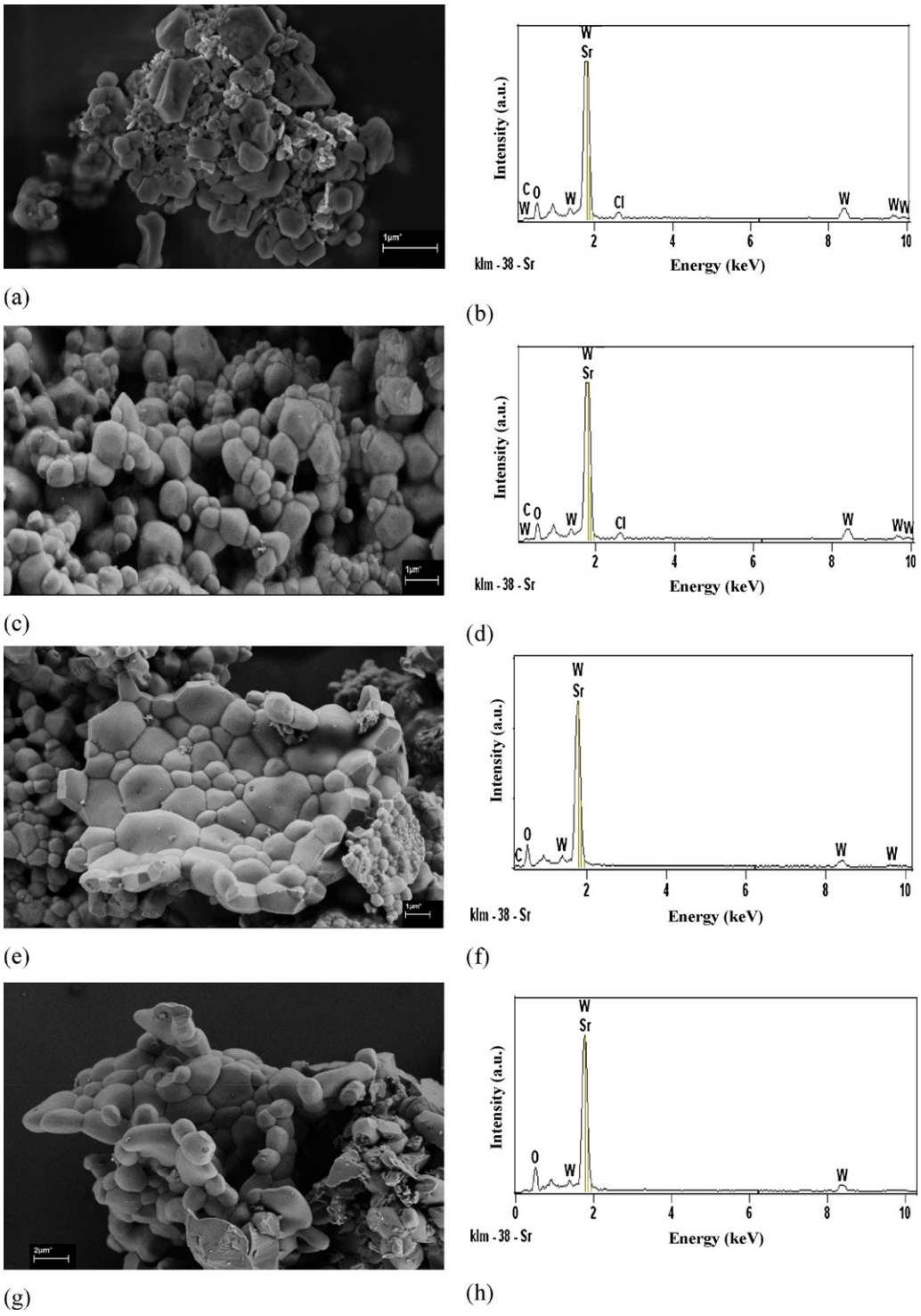

Fig. 6. FEG-SEM micrographs of $SrWO_4$:Eu heat treated at (a) 600 °C, (c) 800 °C, (e) 900 °C and (g) 1000 °C, respectively, processed by non-hydrolytic sol–gel route. (b, d, f, h) EDS of the $SrWO_4$:Eu sample heat treated in different temperatures.

to the stretching and flexion mode of Sr—O. Free rotation modes of $[WO_4]$ are visible at 190.33 and 238.40 cm^{-1}. Vibrational modes are in accordance with analyzed Raman vibrations [35]. Spectra provide evidence for the scheelite structure for all products. According to literature data, all Raman modes observed for $SrWO_4$:Eu obtained in this work are characteristics of the tetragonal structure.

The compounds treated at 600 and 800 °C (see Fig. 5(a) and (b)) show some large peaks of υ_3 (E_g) at 800.95 cm^{-1} which are related to internal modes; peak characteristics of $\upsilon_{f.r.}$ are visible at 102.62 and 76.05 cm^{-1} which are external modes. Broad peaks at 715.98 and 272.56 cm^{-1} are probably due to additional phases which disappear as the annealing temperature increases and indicate that $[WO_4]$ clusters contain distortions on the short-range tetrahedron group. These results seem to be in agreement with the XRD (see Fig. 1(a) and (b)) which shows phase mixtures. Therefore, well defined Raman active modes indicate that $SrWO_4$:Eu powders processed by the non-hydrolytic sol–gel method and at annealing temperatures of 900 and 1000 °C are ordered at short range (see

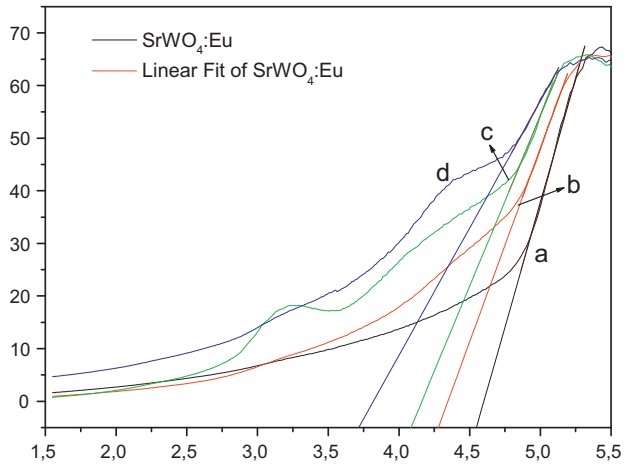

Fig. 7. UV–vis absorbance spectra for the $SrWO_4$:Eu sample heat treated at (a) E_{gap} (600 °C) = 4.55 eV, (b) E_{gap} (800 °C) = 4.28 eV, (c) E_{gap} (900 °C) = 4.08 eV and (d) E_{gap} (1000 °C) = 3.71 eV.

Fig. 5(c) and (d)). Raman spectra for these samples did not represent any significant change which indicates that the addition of 1.0% europium was unable to modify stretching, torsion and bending vibrational modes of W—O bonds since the W atom is located at the B site of the scheelite structure. This behavior is possible only because Eu^{3+} is replacing the Sr^{2+} located at the A site in the $SrWO_4$ matrix.

3.5. FEG-SEM: morphology

Fig. 6(a), (c), (e), and (g) shows FEG-SEM micrographs and EDS spectra ((b), (d), (f), and (h)) of $SrWO_4$:Eu samples heat treated at 600, 800, 900 and 1000 °C, respectively, processed by the non-hydrolytic sol–gel route.

The increase in the annealing temperature contributes to the coalescence process which promotes the growth of aggregated particles of a polydisperse nature [21,33]. According to Fig. 6(a), (c), (e), and (g), an increase in particle sizes and shapes results in self-assemby which originates from the characteristic morphology of the material as plates having different particle size distributions.

A qualitative analysis of the powders obtained was performed using EDS data (see Fig. 6(b), (d), (f), and (h)) which clearly indicates that the samples are composed of Sr, W and O since their peaks were observed as expected. The presence of the C peak due to the upper lying conductive carbon tape is obvious. Samples were doped with 1.0% of Eu^{3+}; thus, due to its low concentration, no europium peak was observed. The Sr signal overlaps with the W signal in the energy scale of ca. 1.9 keV. Fig. 6(b) and (d) shows a peak of Cl which is in agreement with the mixture phase which is ascribed to the tungsten oxychloride ($WOCl_4$) as verified by XRD data (see Fig. 1(a) and (b)). Also in agreement with XRD data and Raman spectra, Fig. 6(f) and (h) did not manifest these signals (see Fig. 1(c) and (d)) which verifies the presence of only $SrWO_4$:Eu crystals.

3.6. UV–vis absorption spectroscopy analyses

The optical band gap energy (E_{gap}) values obtained from the UV–vis spectroscopy are shown in Fig. 7. According to Wood and Tauc [38], the optical band gap energy is related to the absorbance intensity and photon energy:

$$\alpha h\nu = A(h\nu - E_{gap})^{1/n} \quad (2)$$

where α is the absorbance, h is the Planck constant, ν is the frequency and E_{gap} is the optical band gap. Therefore, the optical band gap was determined by extrapolation of the linear portion of the curve or tail. The combination of absorbance and PL measurements reveals energy levels of the materials and the optical band gap value [17].

Fig. 7 shows the UV–vis spectral dependence on absorbance for $SrWO_4$:Eu samples, and these values are listed in Fig. 7; samples were processed by the non-hydrolytic sol–gel route and heat treated at 600, 800, 900 and 1000 °C for 2 h.

These spectra verify that the optical band gap is dependent on the annealing temperature and the degree of structural order or distortion of the lattice. According to the literature [18,20,21,28,31,39–41], the E_{gap} is associated with intermediary energy levels within the material band gap. Fig. 7(a–d) shows that an increase in processing temperature leads to a reduction in the E_{gap}. Wood and Tauc [38] associated this decrease in the gap energy value with intermediate localized states in the band gap due to structural defects. This behavior indicates that the density of localized states in the band gap value of the sample heat treated at 1000 °C is greater than the value obtained for samples treated at other temperatures. The energy gap decreases as structural disorders or distortions increase which is in accordance with Rietveld data.

The absorbance from sample curves of Fig. 7(a) 600 °C and (b) 800 °C reveal a smoother slope than sample curves of Fig. 7(c) 900 °C and (d) 1000 °C which shows absorption tails below the exponential part of the edge. Absorbance measurement for samples annealed at 900 and 1000 °C suggests the absence of a uniform band gap structure with a tail of localized states (see Fig. 7(c) and (d)) and a well defined inter-band transition with a quasi-vertical absorption which is probably related to crystalline effects.

Results between E_{gap} (eV) values of $SrWO_4$ obtained in this work were analyzed and compared with results reported in the literature by different methods. Santos et al. [20] obtained E_{gap} values of 4.7 and 4.5 eV for thin films annealed at 700 and 600 °C for 2 h, respectively. Sczancoski et al. [21] showed E_{gap} values of 4.36, 4.49, 4.59, 4.68, 4.43 eV to powders obtained by a microwave method at 140 °C at 0.5, 1, 2, 5 and 8 h, respectively. Orhan et al. [31] reported E_{gap} values of 5.76 and 4.61 eV for thin films annealed at 600 and 400 °C for 4 h, respectively. Maurera et al. [39] and Lou and Cocivera [40] obtained E_{gap} values of 5.78 and 4.9 eV for thin films annealed at 400 °C for 4 h and 700 °C for 1 h, respectively. We believe that E_{gap} values can also be related with factors such as particle morphology, annealing temperature, processing time, preparation method and shape (thin films or powders) as well as doping.

In $SrWO_4$:Eu phosphors, the Eu^{3+} ion is expected to replace the Sr^{2+} ion it would be difficult to keep a charge balance in the phosphor. When a trivalent metallic ion such as Eu^{3+} is incorporated into a host lattice and substitutes for a divalent metallic ion, charge balancing is necessarily required. The equations to solve the problem of the charge compensation are suggested below [15,42–44]:

$$[SrO_8]^x + [SrO_7{\cdot}V_0{}^x] \rightarrow [SrO_8]' + [SrO_7{\cdot}V_0{}^\bullet] \quad (3)$$

$$[SrO_8]^x + [SrO_7{\cdot}V_0{}^\bullet] \rightarrow [SrO_8]' + [SrO_7{\cdot}V_0{}^{\bullet\bullet}] \quad (4)$$

$$[EuO_8]^\bullet + [SrO_8]' \rightarrow [EuO_8]^x + [SrO_8]^x \quad (5)$$

$$[WO_4]^x + [WO_3{\cdot}V_0{}^x] \rightarrow [WO_4]' + [WO_3{\cdot}V_0{}^\bullet] \quad (6)$$

$$[WO_4]^x + [WO_3{\cdot}V_0{}^x] \rightarrow [WO_4]' + [WO_3{\cdot}V_0{}^{\bullet\bullet}] \quad (7)$$

$$[EuO_8]^\bullet + [WO_4]' \rightarrow [EuO_8]^x + [WO_4]^x \quad (8)$$

In disordered tungstate powders, oxygen vacancies can occur in different charge states such as $[SrO_7{\cdot}V_0{}^x]$, $[WO_3{\cdot}V_0{}^x]$ which capture electrons and are neutral in relation to the lattice as well as singly ionized $[SrO_7{\cdot}V_0{}^\bullet]$, $[WO_3{\cdot}V_0{}^\bullet]$ states and doubly positively charged states in the lattice $[SrO_7{\cdot}V_0{}^{\bullet\bullet}]$, $[WO_3{\cdot}V_0{}^{\bullet\bullet}]$ which do not trap any electrons. These oxygen vacancies induce the appearance of new

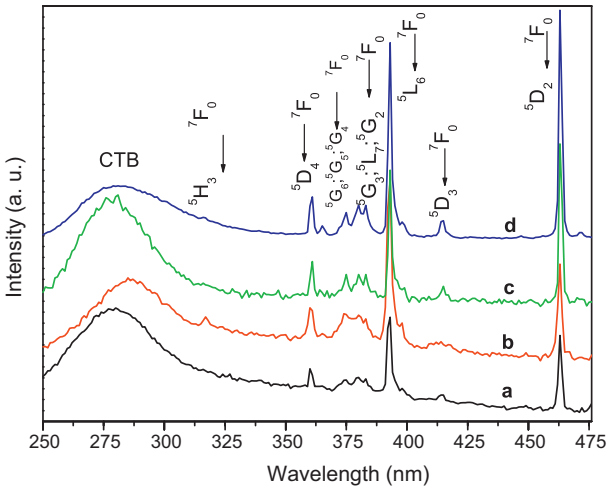

Fig. 8. Excitation spectrum of $SrWO_4$:Eu^{3+} samples heat treated at (a) 600 °C, (b) 800 °C, (c) 900 °C and (d) 1000 °C for 2 h which monitors the $^5D_0 \rightarrow {}^7F_2$ emission at 616 nm performed at a liquid nitrogen temperature of 77 K.

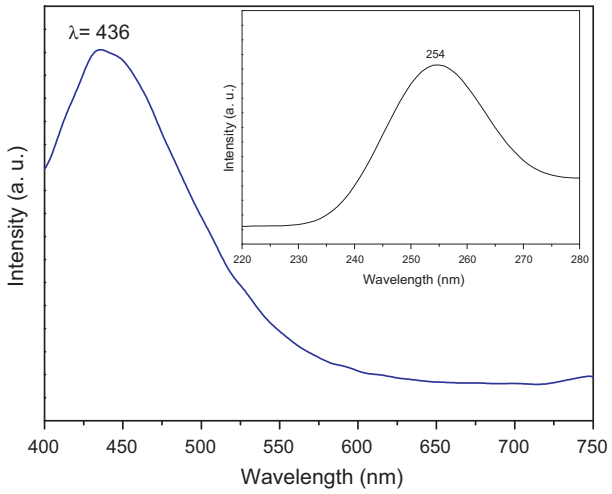

Fig. 9. Emission spectrum ($\lambda_{exc.}$ = 254 nm) of the non-doped $SrWO_4$ sample treated at 800 °C for 2 h. Insert: Excitation spectrum ($\lambda_{em.}$ = 436 nm) recorded at a liquid N_2 temperature.

energy states in the band gap which can be attributed to tungsten and strontium oxygen centers. Before donor excitation, a hole in the acceptor and an electron in a donor are created, according to the Eqs. (3)–(8) above. These equations suggest that the oxygen vacancy trapped electron in the valence band is necessary for the transition of a valence band hole in the conduction band. It must be understood that this is not a band-to-band transition and that the charge transfer depends on intrinsic structural defects in the lattice [15,42–44].

Different mechanisms are responsible for the PL behavior in $SrWO_4$ such as Eu^{3+} disorder or distortion caused by $[SrO_7{\cdot}V_0{}^x]$, $[WO_3{\cdot}V_0{}^x]$, $[SrO_7{\cdot}V_0{}^\bullet]$, $[WO_3{\cdot}V_0{}^\bullet]$ and $[SrO_7{\cdot}V_0{}^{\bullet\bullet}]$, $[WO_3{\cdot}V_0{}^{\bullet\bullet}]$ clusters in disordered structures and an intrinsic distorted $[WO_4]^{2-}$ tetrahedral in a short-range ordered structure. In this case the concentration of the clusters $[EuO_8]^\bullet$ is higher than the $[SrO_8]^x$ one.

3.7. PL

Eu^{3+} PL is sensitive to local lattice symmetry and can be used as an intrinsic probe to map out changes in chemical surroundings regarding lattice dimensions and symmetry for different kinds of nanocrystals [45,46].

Fig. 8 shows excitation spectra of a Eu^{3+}-doped $SrWO_4$ matrix which monitor the Eu^{3+} $^5D_0 \rightarrow {}^7F_2$ emission at 616 nm at a liquid nitrogen temperature of 77 K.

In the 310–475 nm spectral range depicted in Fig. 8, sharp lines are visible due to 4f ↔ 4f transitions assigned to the $^7F_0 \rightarrow {}^5L_J$ (L = D, G, H, L where J = 0–7) of the Eu^{3+} ion transitions for all samples. The main peak is assigned to the $^7F_0$ fundamental to the $^5L_6$ excited state transition (electric dipole) at 393 nm. These narrow lines are assigned to transitions from the $^7F_0$ to the ^5G_J (365–385 nm), $^5L_{6,7}$ (381 and 393 nm), $^5H_3$ (317 nm) and $^5D_{2-4}$ (360, 415 and 462 nm) levels. Spectra have a broad band in the range of 230–320 nm which is attributed to the cluster–cluster charge transfer (CCCT) of oxygen to tungsten and europium ions [47]. Furthermore, it is remarkable that synthesized phosphors can strongly absorb not only in short (~280 nm) and lower (393 nm) UV ranges, but also in the visible (462 nm) energy range [48]. As the annealing temperature increases, the intensity of the f–f transitions increases for the CCCT which indicates a higher crystalline organization of materials. In $SrWO_4$:Eu phosphors, the CCCT from O^{2-} to W^{6+} is ascribed to electron transitions from the oxygen 2p orbital to the empty tungsten 5d orbital or to an empty Eu^{3+} 4f orbital. They are closely related to the coupling between the luminescent centers and the crystal lattice because these couplings mainly depend on the distance from metal ions to ligands [7].

Fig. 9 shows the emission spectrum of the non-doped $SrWO_4$ sample treated at 800 °C for 2 h and monitored under $\lambda_{exc.}$ = 254 nm. The insert shows the excitation spectrum of the same sample monitored at 436 nm; both assays were performed at liquid N_2 temperatures. According to Fig. 9, the undoped $SrWO_4$ sample produces a broad blue emission under UV-light excitation. However, Fig. 10 shows that the blue emission is quenched, and narrow lines are ascribed to Eu^{3+} emission spectra which are intensified due to the introduction of this ion into the $SrWO_4$ matrix [49].

Fig. 9 insert shows a broad and highly intense band at around 254 nm which is assigned to the CCCT of the O → W from $[WO_4]$ units in the pure $SrWO_4$ matrix. In comparison with doped compounds (see Fig. 8), the excitation bands ascribed to the CCCT are shifted to lower energies (~280 nm). This behavior could be associated with the coordination of $WO_4{}^{2-}$ groups with Eu^{3+} ions.

The emission spectrum of the pure $SrWO_4$ sample excited at 254 nm (see Fig. 9) shows a broad blue emission band centered at around 436 nm. This spectrum exhibits a similar behavior when compared to other reported tungstates [47,50].

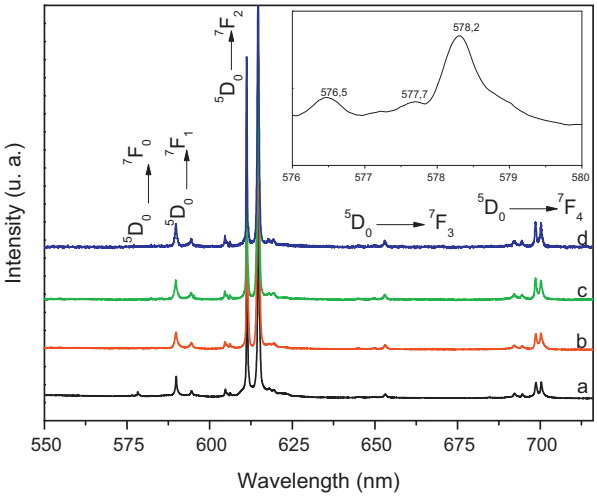

Fig. 10. Emission spectra of $SrWO_4$:Eu^{3+} treated at (a) 600 °C, (b) 800 °C, (c) 900 °C and (d) 1000 °C for 2 h with excitation of 393 nm ($^5L_6$) at 77 K.

Fig. 10 shows emission spectra of $SrWO_4$:Eu treated at (a) 600, (b) 800, (c) 900 and (d) 1000 °C for 2 h with excitation at 393 nm ($^5L_6$) recorded at 77 K.

Emission spectra are similar for all samples and correspond to typical 4f levels specific transitions of Eu^{3+}. The emission spectra were recorded at room temperature and have essentially the same emission profile. However, a higher resolution of the emission bands is observed at 77 K because at this temperature the higher vibrational levels of the lattice are almost depopulated and thus result in a less intense vibronic coupling between matrix vibrational modes and metal electronic states. In these emission spectra, multifold components are attributed to $(2J+1)$ Stark levels of J-degeneracy. The $^5D_0 \rightarrow {}^7F_2$ electric dipole transition is dominant when Eu^{3+} occupies a non-centrosymmetric environment such as in the scheelite framework [51]. Emission spectra of all samples revealed transitions from $^5D_0$ excited levels to ground states ^7F_J (J = 0, 1, 2, 3 and 4) of the Eu^{3+} at around 578, 589, 616, 652 and 699 nm, respectively. The levels with J = 0 are not degenerate, and the $^5D_0 \rightarrow {}^7F_0$ transition shows no more than one band; $^5D_0 \rightarrow {}^7F_1$ three bands; $^5D_0 \rightarrow {}^7F_2$ five bands; $^5D_0 \rightarrow {}^7F_3$ seven bands and $^5D_0 \rightarrow {}^7F_4$ nine bands, if the Eu^{3+} is located in sites having only one kind of symmetry. The sample heated at 600 °C shows three peaks at 576.5, 577.7 and 578.2 nm (see Fig. 10 insert) ascribed to $^5D_0 \rightarrow {}^7F_0$ transitions which suggests more than one site of different symmetry for the chemical environment around Eu^{3+} ions. Samples treated at 800, 900, and 1000 °C show only one peak at 578.8 nm which indicates only one kind of Eu^{3+} symmetry site. Emission spectra with excitation at 462 nm ($^5D_2$) recorded at 77 K and room temperature (not illustrated) have the same emission profile which indicates only one kind of Eu^{3+} symmetry site.

In the tetragonal $SrWO_4$ system, Eu^{3+} ions partially substitute Sr^{2+} ions. The strongest peaks are visible at 616 nm because Eu^{3+} ions are located at non-centrosymmetrical sites [52]. $SrWO_4$:Eu powders show a predominant red emission of the characteristic Eu^{3+} $^5D_0 \rightarrow {}^7F_2$ transition when excited at 393 nm. Eu^{3+} is a good probe for the chemical environment of rare-earth ions since the $^5D_0 \rightarrow {}^7F_2$ transition (electric dipole) is hypersensitive to the surrounding Eu^{3+}environment while the $^5D_0 \rightarrow {}^7F_1$ transition (allowed by magnetic dipole) is insensitive to the environment. In a site with inversion symmetry, the $^5D_0 \rightarrow {}^7F_1$ transition dominates while in a site without inversion symmetry, the $^5D_0 \rightarrow {}^7F_2$ transition dominates. The dominant emission emanates mainly from the parity forbidden electric dipole transition rather than the magnetic dipole transition which indicates that Eu^{3+} ions are located at a non-site symmetry [8,22,53].

As shown in Fig. 10, the blue emission is quenched, and narrow lines ascribed to the Eu^{3+} emission spectra related to the introduction of this ion into the $SrWO_4$ matrix are intensified. We believed that this behavior is due to defects in the framework which forms the vacancy that probably contributes to the arrangement of the lattice. Consequently, the emission ascribed to the matrix is quenched by removing the emission broad band at 436 nm. Oxygen vacancies can occur through the $[EuO_8]^{\bullet}$, $[SrO_8]'$ and $[WO_4]'$ which are neutralized in the lattice as shown in Eqs. (5) and (8).

Table 6 shows the relative area of $^5D_0 \rightarrow {}^7F_0/{}^5D_0 \rightarrow {}^7F_2$ and $^5D_0 \rightarrow {}^7F_2/{}^5D_0 \rightarrow {}^7F_1$ transitions on $SrWO_4$:Eu samples.

Table 6
Relative area of $^5D_0 \rightarrow {}^7F_0/{}^5D_0 \rightarrow {}^7F_2$ and $^5D_0 \rightarrow {}^7F_2/{}^5D_0 \rightarrow {}^7F_1$ transitions on the $SrWO_4$:Eu samples heat treated at 600, 800, 900 and 1000 °C for 2 h.

$SrWO_4$:Eu	$^5D_0 \rightarrow {}^7F_0/{}^5D_0 \rightarrow {}^7F_2$	$^5D_0 \rightarrow {}^7F_2/{}^5D_0 \rightarrow {}^7F_1$
600 °C	0.039	5.8
800 °C	0.0003	11.7
900 °C	0.0006	11.2
1000 °C	0.0008	9.8

The ratio of the $(^5D_0 \rightarrow {}^7F_2)/(^5D_0 \rightarrow {}^7F_1)$ emission intensity provides valuable information about the symmetry of the site where Eu^{3+} ions are situated. Emission spectra of powders showed a marked increase in intensities as the heat temperature increases during the synthesis process.

A ratio between the integrated intensity these two transitions, I_{0-2}/I_{0-1}, is used in lanthanide-based systems as a probe to evaluate local cation surroundings [54] (see Table 6). The higher variation of the I_{0-2}/I_{0-1} ratio of the sample annealed at 600 °C as compared to the other samples is an indication of the Eu^{3+} structural change to a higher symmetry which generates breaks in symmetry systems and produces intermediary levels within the band gap which causes differences in the luminescence behavior of these materials. The I_{0-2}/I_{0-1} ratio for samples treated at 800, 900 and 1000 °C did not show variations between these values which indicates that Eu^{3+} ions have lower symmetry in relation to sample heated at 600 °C for 2 h. The I_{0-0}/I_{0-2} intensity parameter ratio between intensities of the $^5D_0 \rightarrow {}^7F_0$ and $^5D_0 \rightarrow {}^7F_2$ transitions was determined for $SrWO_4$:Eu samples annealed at different temperatures as compared to Refs. [55,56]. The I_{0-0}/I_{0-2} parameter may give information on the J-mixing effect associated with the $^5D_0 \rightarrow {}^7F_0$ transition as described in Ref. [57]. This effect is mainly due to mixing between the $^7F_2$ manifold and the $^7F_0$ level through two rank components of the chemical environment around the rare earth ion. $SrWO_4$:Eu samples annealed at 800, 900 and 1000 °C had similar I_{0-0}/I_{0-2} value-based complexes and polymers (these systems show a much smaller value than the value obtained in Refs. [55,56]). However, for $SrWO_4$:Eu samples annealed at 600 °C for 2 h, a higher value is observed than the value for $SrWO_4$:Eu samples annealed at different temperatures as well as different complexes and polymers [55,56] which indicates a much higher magnitude of the J-mixing effect.

The intensity of a forced electric dipole $^5D_0 \rightarrow {}^7F_2$ transition is strongly sensitive to the nature of the Eu^{3+}-ligand surroundings and increases as the site symmetry of the Eu^{3+} center decreases. The increase in the hypersensitive I_{0-2}/I_{0-1} ratio was ascribed previously to an increase in both the covalence and the polarization in the local vicinities of the Eu^{3+} cations in short-range effects.

3.7.1. Lifetime

On the basis of emission spectra and lifetimes of the $^5D_0$ emitting level, the quantum efficiency, η, of $^5D_0$ for Eu^{3+} ions in $SrWO_4$:Eu nanocrystals can be determined.

According to literature publication [47], the lifetime (τ), nonradiative (A_{nrad}) and radiative (A_{rad}) rates are related through the following equation: $A_{tot} = 1/\tau = A_{RAD} + A_{NRAD}$, where the A_{RAD} rate was obtained by summing over the radiative rates A_{0J} for each $^5D_0 \rightarrow {}^7F_J$ transition is given by $A_{RAD} = \sum_J A_{0J}$. The emission quantum efficiency of the emitting $^5D_0$ level is given by:

$$\eta = \frac{A_{RAD}}{A_{RAD} + A_{NRAD}} \quad (9)$$

Fig. 11 shows decay curves of the Eu^{3+} $^5D_0 \rightarrow {}^7F_2$ transition in $SrWO_4$ samples heat treated at (a) 600, (b) 800, (c) 900 and (d) 1000 °C where excitation and emission wavelengths were fixed at 394 and 616 nm, respectively.

The curve (a) shows the fit of the bi-exponential function to a sample heat treated at 600 °C (τ_1 = 0.84 and τ_2 = 0.05 ms, second order) and mono exponential function to samples heat treated at 800, 900 and 1000 °C (τ = 0.71, τ = 0.64 and τ = 0.65 ms), respectively which verified that these values are in agreement with emission spectra (see Fig. 10). Changes in the environment can cause only a slight change in the position of electronic transition lines of rare earth. However, different values in its luminescence lifetime have been observed [58]. Eu^{3+} decay times for samples were evaluated from these decay curves (see Table 7). Table 7 shows the lifetime

Table 7
Experimental intensity parameters (Ω_λ), emission quantum efficiencies (η), lifetime (τ), non-radiative (A_{nrad}), radiative (A_{rad}) and chromaticity (x and y) for the $SrWO_4$:Eu sample at room temperature.

	τ (ms)	A_{RAD} (s^{-1})	A_{NRAD} (s^{-1})	η (%)	Ω_2 ($\times10^{-20}$ cm^2)	Ω_4 ($\times10^{-20}$ cm^2)	Chromaticity	
							x	y
600 °C	–	–	–	–	–	–	0.669	0.328
800 °C	0.71	792	617	56	25.7	7.12	0.673	0.326
900 °C	0.64	777	785	50	24.8	7.51	0.683	0.315
1000 °C	0.65	693	845	45	21.7	7.12	0.681	0.318

tendency due to temperature. A decrease in the lifetime of the $^5D_0 \rightarrow {}^7F_2$ transition was observed due to temperature which can be explained by sample sinterization.

Quantum efficiencies for samples heat treated at 800, 900 and 1000 °C were evaluated as 56%, 50% and 45%, respectively. It is clear that the quantum efficiency of samples heat treated at 800 °C is higher the quantum efficiency for samples at 900 and 1000 °C which seems to be consistent with the longer lifetime of the sample at 800 °C (τ = 0.71 ms) (see Table 7). The enhanced quantum efficiency and the increased lifetime for a sample at 800 °C could be interpreted as a decrease in the non-radiative combination centers of the Eu^{3+} ions which strongly contributes to multiphonon deactivation at the $^5D_0$ level. This level is almost depopulated which lowers the rate of vibronic coupling and results in an increase in the Eu^{3+} emission luminescence lifetime. The relatively short lifetime determined for the samples heat treated at 900 and 1000 °C at room temperature (τ = 0.64 and 0.65 ms), respectively, is a consequence of the large number of high energy vibrational oscillators around Eu^{3+} ions. Non-radiative combination centers can be produced by factors such as defects and surface states where these defects may serve as non-radiative recombination centers for decreased quantum efficiency which is in accord with the E_{gap} (see Fig. 7) that decreases with a temperature increase.

3.7.2. Intensity parameters

The luminescence behavior of the Eu^{3+} ion into $SrWO_4$ can be investigated by radiative and non-radiative contributions to decay rates from the emitting level such as $^5D_0$ using the $^5D_0 \rightarrow {}^7F_2$ and $^5D_0 \rightarrow {}^7F_4$ transitions [47]. It is important to study the influence of the tungstate anion on the europium luminescence behavior by determining the radiative contribution of the emitting level depopulation, $^5D_0$, and consequently for the emission quantum efficiency.

In this case, spectral data at room temperature must be considered by using $^5D_0 \rightarrow {}^7F_2$ and $^5D_0 \rightarrow {}^7F_4$ transitions of the Eu^{3+} ion

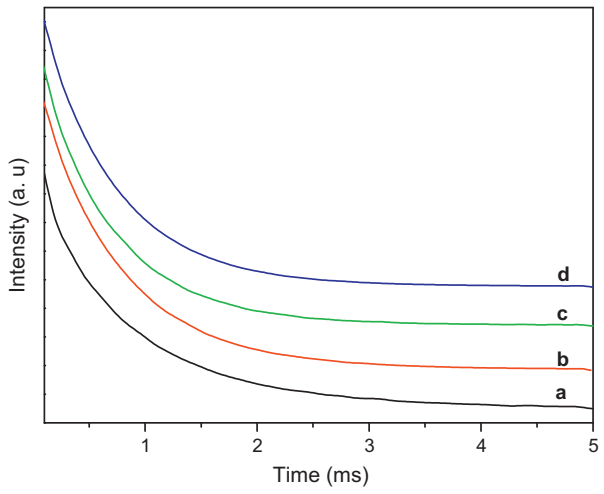

Fig. 11. Decay curves of the Eu^{3+} emission ($\lambda_{em.}$ = 616 nm, $\lambda_{ex.}$ = 393 nm) for $SrWO_4$ samples heat treated at (a) 600 °C, (b) 800 °C, (c) 900 °C and (d) 1000 °C.

to determine the Ω_λ (λ = 2 and 4) experimental intensity parameters by taking the $^5D_0 \rightarrow {}^7F_1$ transition as the reference. Thus experimental intensity parameters (Ω_λ) of the $SrWO_4$:Eu systems were determined through the ratio between the intensities of the $^5D_0 \rightarrow {}^7F_{2,4}$ and $^5D_0 \rightarrow {}^7F_1$ transitions. The $^5D_0 \rightarrow {}^7F_1$ transition is taken as the reference due to its predominant magnetic dipole character. The hypersensitive $^5D_0 \rightarrow {}^7F_2$ transition is forbidden by magnetic dipole and allowed by electric dipole mechanism.

The calculations were obtained based on Refs. [47,59], through the equation:

$$A_{0-\lambda} = \frac{4e^2\varpi^3}{3\hbar c^3}\chi\sum_{\lambda=2,4}\Omega_\lambda\left\langle {}^5D_0\left|U^{(\lambda)}\right|{}^7F_J\right\rangle^2, \quad (10)$$

where $\chi = n_0(n_0^2+2)^2/9$ is the Lorentz local field correction. The square reduced matrix elements are $\left\langle {}^5D_0\left|U^{(2)}\right|{}^7F_2\right\rangle^2 = 0.0032$ and $\left\langle {}^5D_0\left|U^{(4)}\right|{}^7F_4\right\rangle^2 = 0.0023$, while the average index of refraction is 1.5. The $A_{0-\lambda}$ values are obtained according the relation presented at Eq. (11):

$$A_{0-\lambda} = A_{0-1}\left(\frac{S_{0-\lambda}}{S_{0-1}}\right)\left(\frac{\sigma_\lambda}{\sigma_1}\right) \quad (11)$$

where $S_{0-\lambda}$ is the area of the band related to the $^5D_0 \rightarrow {}^7F_\lambda$ transition obtained from the spectral data, σ_λ is the barycenter of the 0–λ transition and $A_{0-\lambda}$ is Einstein's coefficient for the 0–1 magnetic dipole transition. The $A_{0,1}$ value is estimated to be 50 s^{-1}.

Tables 7 and 8 shows Ω_λ intensity parameter values (λ = 2 and 4) for $SrWO_4$:Eu compounds. When a comparison is made between Ω_2 parameters for all compounds, the values are very close which indicates that the Eu^{3+} ion is in a similar polarizable environment and that the covalent character of the metal–donor atom interaction is also similar for these ions. Comparing Ω_λ intensity parameters values with other RE^{3+}-complexes and other RE^{3+}-matrices, the chemical environment around rare earth ions in tungstate systems is less polarizable than the $Eu(TTA)_3{\cdot}2H_2O$, $Eu(TTA)_3{\cdot}2DBSO$, polymer which suggests a smaller electric dipole character for the $^5D_0 \rightarrow {}^7F_2$ transition. Parra and Malta [55,56] observed high Ω_2 values (20–40 $\times$ 10^{-20} cm^2) in epoxy resin and rare earth complexes which reflects the hypersensitive behavior of the $^5D_0 \rightarrow {}^7F_2$ transition. Nevertheless, the europium ion in $SrWO_4$:Eu (see Table 7) is in a more polarizable environment than YAG:Eu^{3+} samples (see Table 8) because Ω_2 parameter values are ~25 $\times$ 10^{-20} cm^2 and 1.64 $\times$ 10^{-20} cm^2, respectively which indicates the significant covalent character of the metal–donor atom interaction in europium tungstate compounds. The Ω_2 value which

Table 8
Experimental intensity parameters (Ω_λ) for the $Eu(TTA)_3{\cdot}2H_2O$, $Eu(TTA)_3{\cdot}2DBSO$, polymer 10% and YAG:Eu^{3+} samples at room temperature.

	Ω_2 ($\times10^{-20}$ cm^2)	Ω_4 ($\times10^{-20}$ cm^2)	Ref.
$Eu(TTA)_3{\cdot}2H_2O$	33	4.6	[55,56]
$Eu(TTA)_3{\cdot}2DBSO$	29	3.5	[56]
Polymer	35.4	9.9	[55]
YAG:Eu^{3+}	1.64	5.61	[12]

depends on the degree of covalence experienced by the metal (higher Ω_2 values correspond to higher covalences) attests to a highly covalence character for bonds established in the compounds studied in this work.

Tables 7 and 8 show the Ω_4 experimental intensity parameter values with the highest value for the $SrWO_4$:Eu sample which indicates the high sensitivity behavior of the $^5D_0 \rightarrow {}^7F_4$ transition. In the tungstate system, $\Omega_2 > \Omega_4$ parameters suggest that the coordination geometry is higher, and the site symmetry occupied by the Eu^{3+} ion in the tungstate system does not have a centrosymmetric chemical environment character since the $^5D_0 \rightarrow {}^7F_2$ transition is formally forbidden due to the electric dipole selection rule [47,59]. Table 8 shows that YAG:Eu^{3+} has lower Ω_2 values which indicates a weak chemical Eu—O polarization environment.

The chromaticity coordinates at room temperature for $SrWO_4$:Eu compounds heat treated at 600, 800, 900 and 1000 °C are ($x = 0.669$, $y = 0.328$), ($x = 0.673$, $y = 0.326$), ($x = 0.683$, $y = 0.315$) and ($x = 0.681$, $y = 0.318$), respectively (see Table 7). The sample color coordinates are well fitted in the red region which corresponds to the $^5D_0 \rightarrow {}^7F_2$ europium ion emission. These chromaticity coordinates are excellent for a red phosphor and indicate that they are comparable to commercially available red phosphor coordinates used for cathode ray tubes as Y_2O_2S:Eu^{3+}; where $x = 0.64$, $y = 0.34$) [47].

4. Conclusions

Crystalline scheelite $SrWO_4$:Eu phosphors were prepared by using a non-hydrolytic sol–gel route; this methodology is more efficient in the doping of Eu^{3+} ions than a traditional solid-state reaction because it promotes the mixture of the starting materials at the molecular level. Besides $SrWO_4$:Eu was successfully prepared by this method at temperatures below those mentioned in the literature.

XRD and vibrational and optical studies showed that the structure of the synthesized $SrWO_4$:Eu scheelite type was formed at 900 and 1000 °C for 2 h. Raman spectra indicated only one kind of [WO_4] tetrahedra; lattice parameters and the cell volume of samples heat treated at 900 and 1000 °C for 2 h verify that an increase in the temperature decreases lattice parameters and cell volumes and cause only a slightly environment distortion rather than significant changes. The ionic radius of Eu^{3+} (0.107 nm) is slightly lower than the ionic radius of Sr^{2+} (0.113 nm) which results in lower lattice parameters. This small difference in lattice parameters is an indication that the addition of Eu^{3+} ion leads to a substitution in the A site occupied by the Sr atoms. PL is a complementary technique for XRD and Raman spectroscopy on the characterization of these materials in a short-, medium- and long-range order. Excitation and emission spectra, decay curves and the dependence of luminescence on the temperature were studied. In emission spectra, the strongest emission is the electric dipole transition red emission $^5D_0 \rightarrow {}^7F_2$ (616 nm) while the magnetic dipole transition orange emissions $^5D_0 \rightarrow {}^7F_{1,3}$ (589 and 652 nm) are subordinated. PL properties, the calculus of the relative area of the $^5D_0 \rightarrow {}^7F_2/{}^5D_0 \rightarrow {}^7F_1$ transitions of the Eu^{3+} ion and the calculus of the emission quantum efficiencies (η) and lifetimes (τ) prove that the materials were formed because the strongest peak at 616 nm is due to Eu^{3+} ions in a site without inversion symmetry. These results are in agreement with XRD, refinement data, Raman spectroscopy and E_{gap} values. A rationale for observed changes related to UV–vis and luminescence spectra is proposed to study the nanocrystals obtained. Luminescence data and CIE chromaticity coordinates show that the $SrWO_4$:Eu material is a potential red phosphor for the fabrication of lighting devices based on near-UV or blue LED which can be excited at around 363 and 462 nm. $SrWO_4$:Eu compounds have higher Ω_2 parameter values compared with the YAG:Eu^{3+} system but lower values than the $Eu(TTA)_3 \cdot 2H_2O$, $Eu(TTA)_3 \cdot 2DBSO$, polymer which reflect a highly polarizable chemical environment around Eu^{3+} ion in these samples.

Acknowledgements

The authors acknowledge to FAPESP, CNPq and CAPES (Brazilian research funding agencies) for financial support.

References

[1] C.A. Kodaira, H.F. Brito, E.E.S. Teotônio, M.C.F.C. Felinto, O.L. Malta, G.E.S. Brito, J. Braz. Chem. Soc. 15 (2004) 890.
[2] J.K. Tyminski, C.M. Lawson, R.C. Powell, J. Chem. Phys. 77 (1982) 4318.
[3] F. Cornacchia, A. Toncelli, M. Tonelli, E. Cavalli, E. Bovero, N. Magnani, J. Phys. Condens. Matter 16 (2004) 6867.
[4] Y. Su, L. Li, G. Li, Chem. Mater. 20 (2008) 6060.
[5] T.M. Mazzo, M.L. Moreira, I.M. Pinatti, F.C. Picon, E.R. Leite, I.L.V. Rosa, J.A. Varela, L.A. Perazolli, E. Longo, Opt. Mater. 32 (2010) 990.
[6] C. Guo, T. Chen, L. Luan, W. Zhang, D. Huang, J. Phys. Chem. Solids 69 (2008) 1905.
[7] S. Shi, J. Gao, J. Zhou, Opt. Mater. 30 (2008) 1616.
[8] S. Shi, X. Liu, J. Gao, J. Zhou, Spectrochim. Acta Part A 69 (2008) 396.
[9] E.J. Nassar, L.R. Ávila, P.F.S. Pereira, C. Mello, O.J. Lima, K.J. Ciuffi, L.D. Carlos, Lumin. J. 111 (2005) 159.
[10] E.J. Nassar, L.R. Ávila, P.F.S. Pereira, O.J. Lima, L.A. Rocha, C. Mello, K.J. Ciuffi, L.D. Carlos, Quim. Nova 28 (2005) 238.
[11] P.F.S. Pereira, J.M.A. Caiut, S.J.L. Ribeiro, Y. Messaddeq, K.J. Ciuffi, L.A. Rocha, E.F. Molina, E.J. Nassar, J. Lumin. 126 (2007) 378.
[12] E.J. Nassar, P.F.S. Pereira, E.C.O. Nassor, L.R. Ávila, K.J. Ciuffi, P.S. Calefi, J. Mater. Sci. 42 (2007) 2244.
[13] P.F.S. Pereira, M.G. Matos, L.R. Ávila, E.C.O. Nassor, A.C. Cestari, K.J. Ciuffi, P.S. Calefi, E.J. Nassar, J. Lumin. 130 (2010) 488.
[14] L.S. Cavalcante, J.C. Sczancoski, J.W.M. Espinosa, J.A. Varela, P.S. Pizani, E. Longo, J. Alloys Compd. 474 (2009) 195.
[15] A.B. Campos, A.Z. Simões, E. Longo, J.A. Varela, V.M. Longo, A.T. Figueiredo, F.S. Vicente, A.C. Hernandes, Appl. Phys. Lett. 91 (2007) 051923–51931.
[16] Q. Shao, H. Li, K. Wu, Y. Dong, J. Jiang, J. Lumin. 129 (2009) 879.
[17] J.C. Sczancoski, L.S. Cavalcante, M.R. Joya, J.A. Varela, P.S. Pizani, E. Longo, Chem. Eng. J. 140 (2008) 632.
[18] J.C. Sczancoski, M.D.R. Bomio, L.S. Cavalcante, M.R. Joya, P.S. Pizani, J.A. Varela, E. Longo, M.S. Li, J.A. Andrés, J. Phys. Chem. C 113 (2009) 5812.
[19] M.A. Santos, E. Orhan, M.A.M.A. Maurera, L.G.P. Simões, A.G. Souza, P.S. Pizani, E.R. Leite, J.A. Varela, J. Andrés, A. Beltrán, E. Longo, Phys. Rev. B 75 (2007) 165105–165111.
[20] M.A. Santos, F.C. Picon, M.T. Escote, E.R. Leite, P.S. Pizani, J.A. Varela, E. Longo, Appl. Phys. Lett. 88 (2006) 211913–211921.
[21] J.C. Sczancoski, L.S. Cavalcante, M.R. Joya, J.W.M. Espinosa, P.S. Pizani, J.A. Varela, E. Longo, J. Colloid Interface Sci. 330 (2009) 227.
[22] J. Liu, H. Lian, C. Shi, Opt. Mater. 29 (2007) 1591.
[23] L. Zhou, J. Wei, J. Wu, F. Gong, L. Yi, J. Huang, J. Alloys Compd. 476 (2009) 390.
[24] X. Li, Z. Yang, L. Guan, Q. Guo, Mater. Lett. 63 (2009) 1096.
[25] X. He, M. Guan, N. Lian, J. Sun, T. Shang, J. Alloys Compd. 492 (2010) 452.
[26] J.P. Sattler, J. Nemarich, Phys. Rev. B 1 (1970) 4249.
[27] K.-S. Hwang, S. Hwangbo, J.-T. Kim, Ceram. Int. 35 (2009) 2517.
[28] L.S. Cavalcante, J.C. Sczancoski, V.C. Albarici, J.M.E. Matos, J.A. Varela, E. Longo, Mater. Sci. Eng. B 150 (2008) 18.
[29] http://www.crystalimpact.com/diamond/,. Accessed 14 February 2011.
[30] G. Bergerhoff, M. Berndt, K. Brandenburg, J. Res. Natl. Inst. Stand. Technol. 101 (1996) 221.
[31] E. Orhan, M.A. Santos, M.A.M.A. Maurera, F.M. Pontes, C.O.P. Santos, A.G. Souza, J.A. Varela, P.S. Pizani, E. Longo, Chem. Phys. 312 (2005) 1.
[32] L.S. Cavalcante, J.C. Sczancoski, R.L. Tranquilin, M.R. Joya, P.S. Pizani, J.A. Varela, E. Longo, J. Phys. Chem. Solids 69 (2008) 2674.
[33] L.S. Cavalcante, J.C. Sczancoski, L.F. Lima, J.W.M. Espinosa, P.S. Pizani, J.A. Varela, E. Longo, Cryst. Growth Des. 9 (2009) 1002.
[34] S. Nishigaki, S. Yano, H. Kato, T. Nonomura, J. Am. Ceram. Soc. 71 (1988) C11.
[35] A.P. de Moura, R.C. Lima, M.L. Moreira, D.P. Volanti, J.W.M. Espinosa, M.O. Orlandi, P.S. Pizani, J.A. Varela, E. Longo, Solid State Ionics 181 (2010) 775.
[36] Z.C. Ling, H.R. Xia, D.G. Ran, F.Q. Liu, S.Q. Sun, J.D. Fan, H.J. Zhang, J.Y. Wang, L.L. Yu, Chem. Phys. Lett. 426 (2006) 85.
[37] Y. Mao, S.S. Wong, J. Am. Chem. Soc. 126 (2004) 15245.
[38] D.L. Wood, J. Tauc, Phys. Rev. B 5 (1972) 3144.
[39] M.A.M.A. Maurera, A.G. Souza, L.E.B. Soledade, F.M. Pontes, E. Longo, E.R. Leite, J.A. Varela, Mater. Lett. 58 (2004) 727.
[40] Z. Lou, M. Cocivera, Mater. Res. Bull. 37 (2002) 1573.
[41] S.K. Arora, B. Chudasama, Cryst. Res. Technol. 41 (2006) 1089.
[42] D.P. Volanti, I.L.V. Rosa, E.C. Paris, C.A. Paskocimas, P.S. Pizani, J.A. Varela, E. Longo, Opt. Mater. 31 (2009) 995.
[43] A.P.A. Marques, V.M. Longo, D.M.A. de Melo, P.S. Pizani, E.R. Leite, J.A. Varela, E. Longo, J. Solid State Chem. 181 (2008) 1249.
[44] L.S. Cavalcante, M.F.C. Gurgel, A.Z. Simões, E. Longo, J.A. Varela, M.R. Joya, P.S. Pizani, Appl. Phys. Lett. 90 (2007) 011901–11911.

[45] F. Zhang, M.Y. Sfeir, J.A. Misewich, S.S. Wong, Chem. Mater. 20 (2008) 5500.
[46] F. Zhang, Y. Yiu, M.C. Aronson, S.S. Wong, J. Phys. Chem. C 112 (2008) 14816.
[47] C.A. Kodaira, H.F. Brito, M.C.F.C. Felinto, J. Solid State Chem. 171 (2003) 401.
[48] M.M. Haque, H.-I. Lee, D.-K. Kim, J. Alloys Compd. 481 (2009) 792.
[49] Y. Hu, W. Zhuang, H. Ye, D. Wang, S. Zhang, X. Huang, J. Alloys Compd. 390 (2005) 226.
[50] C. Zhu, S. Xiao, J. Ding, X. Yang, R. Qiang, Mater. Sci. Eng. B 150 (2008) 95.
[51] F.-B. Cao, Y.-W. Tian, Y.-J. Chen, L.-J. Xiao, Q. Wu, J. Lumin. 129 (2009) 585.
[52] J. Wang, X. Jing, C. Yan, J. Lin, F. Liao, J. Lumin. 121 (2006) 57.
[53] F. Lei, B. Yan, J. Phys. Chem. C 113 (2009) 1074.
[54] L.-Y. Zhou, J.-S. Wei, F.-Z. Gong, J.-L. Huang, L.-H. Yi, J. Solid State Chem. 181 (2008) 1337.
[55] D.F. Parra, H.F. Brito, J.D. Matos, L.C. Dias, J. Appl. Polym. Sci. 83 (2002) 2716.
[56] O.L. Malta, H.F. Brito, J.F.S. Menezes, F.R.G. Silva, S.A. Junior, F.S.F. Junior, A.V.M. de Andrade, J. Lumin. 75 (1997) 255.
[57] O.L. Malta, W.M. Azevedo, E.G. Araújo, G.F. Saĭ, J. Lumin. 26 (1982) 337.
[58] I.L.V. Rosa, A.P.A. Marques, M.T.S. Tanaka, D.M.A. Melo, E.R. Leite, E. Longo, J.A. Varela, J. Fluoresc. 18 (2008) 239.
[59] C.A. Kodaira, H.F. Brito, O.L. Malta, O.A. Serra, J. Lumin. 101 (2003) 11.